1    27 September 2016

# 3    Improved retrieval of land ice topography from CryoSat-2 data and its

# 4    impact for volume change estimation of the Greenland Ice Sheet

5    Johan Nilsson[1], Alex Gardner[1], Louise Sandberg Sørensen[2] and Rene Forsberg[2]

6    [1]Jet Propulsion Laboratory, California University of Technology

7    [2]DTU Space, National Space Institute, Technical University of Denmark

## 8    Abstract

9    A new methodology for retrieval of glacier and ice sheet elevations and elevation changes from

10    CryoSat-2 data is presented. Surface elevations and elevation changes determined using this

11    approach show significant improvements over ESA's publically available Cryosat-2 elevation

12    product (L2 Baseline-B), compared to near-coincident airborne laser altimetry from NASA's

13    Operation IceBridge and seasonal height amplitudes from the Ice, Cloud, and Elevation Satellite

14    (ICESat).

15         Applying this methodology to CryoSat-2 data collected in Interferometric Synthetic

16    Aperture mode over the high relief regions of the Greenland ice sheet we find an improvement

17    in the root-mean-square-error (RMSE) of 27% and 40% compared to ESA's L2 product in the

18    derived elevation and elevation changes, respectively. In the interior part of the ice sheet, where

19    CryoSat-2 operates in Low Resolution Mode, we find an improvement in the RMSE of 68% and

20    55% in the derived elevation and elevation changes, respectively. There is also an 86%

21    improvement in the magnitude of the seasonal amplitudes when compared to amplitudes

22    derived from ICESat data. These results indicate that the new methodology provides improved

23    tracking of the snow/ice surface with lower sensitivity to changes in near-surface dielectric

24    properties.

25         To demonstrate the utility of the new processing methodology we produce elevations,

26    elevation changes and total volume changes from Cryosat-2 data for Greenland Ice Sheet

27    during the period Jan-2011 to Jan-2015. We find that the Greenland Ice Sheet decreased in

28    volume at rate of 289 ± 20 $km^3 a^{-1}$, with high inter-annual variability and spatial heterogeneity in

29    rates of loss. This rate is 65 $km^3 a^{-1}$ more negative than rates determined from ESA's L2

30    product, highlighting the importance of Cryosat-2 processing methodologies.

31    1 - Introduction

32    The European Space Agency (ESA) launched CryoSat-2 in April 2010 tasked with monitoring

33    the changes of the Earth's land and sea ice. CryoSat-2 carries a new type of Doppler/delay

34    radar altimeter (Raney, 1998) referred to as SIRAL (SAR Interferometric Radar Altimeter).

35    SIRAL operates in two different modes over land ice. Over the interior part of the ice sheets it

36    operates as a conventional pulse limited radar system, referred to as the "Low Resolution

37    Mode" (LRM). In more complex high-sloping terrain the system uses a novel second antenna to

38    operate in "Interferometric Synthetic Aperture Radar" (SIN) mode. These new features allow the

39    satellite to monitor changes in complex terrain including ice caps, glaciers and the high relief

40    marginal areas of the ice sheets. Such areas are sensitive to changes in climate and contribute

41    greatly to current rates of sea level rise (e.g., Gardner et al. (2013) and Shepherd et al. (2012)).

42         Ku-band radar altimeters are insensitive to cloud cover providing superior coverage to

43    laser altimeters (e.g., ICESat) but experience significant amounts of volume scattering, which is

44    controlled by the time-evolving dielectric properties of the near-surface snow, firn, and ice

45    (Lacroix et al., 2008; Remy et al., 2012). These effects can have large implications for the

46    determination of mass change over a wide range of both spatial and temporal scales. Changing

47    snow conditions can introduce time-varying biases in the data that, in combination with the radar

48  signals interaction with the surface, introduce large elevation biases (0.5 - 1 m) (Nilsson et al.,

49  2015a). This, combined with other factors such as processing methodology and surface

50  topography, makes it difficult to measure small changes for much of the word's ice covered

51  regions (Arthern et al., 2001; Gray et al., 2015; Nilsson et al., 2015b).

52      The mitigation of these effects in the processing of radar altimetry data is required for

53  improved accuracy of derived temporal and spatial changes in surface elevation of glaciers and

54  ice sheets. Several studies have proposed different approaches to assess these effects and

55  improve the retrieval process of surface elevation and elevation changes from radar altimetry

56  data. These include different approaches to waveform retracking (Davis, 1993, 1997; Gray et

57  al., 2015; Helm et al., 2014) and empirical corrections to the estimated surface elevation

58  changes (Davis and Ferguson, 2004; Flament and Rémy, 2012; Sørensen et al., 2015;

59  Wingham et al., 2006b; Zwally et al., 2005, 2011). Relatively little work has been done to assess

60  methods for improving elevation and elevation changes derived from ESA's CryoSat-2 data

61  (Abulaitijiang et al., 2015; Gray et al., 2013, 2015; Helm et al., 2014).

62      Here we conduct a thorough analysis of CryoSat-2 SIN and LRM waveform retracking

63  and geolocation methodologies to design an optimal processing methodology for CryoSat-2

64  elevation retrieval over both smooth and complex ice-covered terrain. We then analyze several

65  different approaches to determining surface elevation and volume changes from the scattered

66  CryoSat-2 elevation retrievals. The overarching goal of this work is to develop robust and

67  accurate elevation retrieval algorithms that are less sensitive to changes in surface and sub-

68  surface scattering properties.

69      The new processing scheme is applied to estimate elevation and volume changes of the

70  Greenland Ice Sheet for the period January 2011 to January 2015, using two independent

71  methods to characterize the robustness of the results due to methodology. The results are

72  compared to change estimates obtained from the ESA L2 Baseline-B surface elevation product

73  (Bouzniac et al., 2014), high accuracy airborne data from NASA IceBridge airborne topographic

74    mapper and seasonal height amplitudes estimated from Ice, Cloud, and Elevation Satellite

75    (ICESat) data.

76    ## 2 - Surface elevations from CryoSat-2

77    ### 2.1 - Low Resolution Mode (LRM)

78    The LRM mode is used over the interior parts of the ice sheet, which mostly consist of low

79    sloping terrain. Here, SIRAL operates as a conventional pulse limited radar system with a

80    transmission frequency of 13.6 GHz (Ku-band) and has Pulse-Limited Footprint (PLF) radius of

81    approximately 1.5 km and a beam-limited footprint (BLF) radius of approximately 7.5 km over

82    flat terrain (Bouzinac, 2014). The gentle terrain allows for accurate mapping of the surface

83    elevation of the ice sheet down to decimeter-level (Brenner et al., 2007). Within the LRM

84    waveform we define the location of the surface from the leading edge of the waveform, based

85    on a fraction of the maximum amplitude of the received power. This approach is commonly

86    referred to as a threshold retracker. Following Davis et al. (1997) we use 20% threshold to

87    define the location of the surface. Davis et al. (1997) argued that a 20% threshold represents

88    the best compromise between waveforms that are entirely dominated by either volume or

89    surface scattering, making it suitable for obtaining estimates of surface elevation for most parts

90    of the Greenland Ice Sheet.

91        The CryoSat-2 LRM radar waveforms suffer from measurement noise, in the form of

92    speckle noise. Furthermore, over the steeper parts of the LRM-area the range gate tracking-

93    loop can loose track of the surface, producing non-usable waveforms. To remove bad or loss of

94    track waveforms the radar waveform (20 Hz) is first filtered using a zero-phase low pass filter to

95    reduce speckle noise on a line-by-line basis. The signal-to-noise-ratio (SNR) of the waveform is

96    then estimated and if the SNR < 0.5 dB the waveform is rejected. The SNR threshold was

97      empirically chosen to obtain a good trade-off between the quality of the measurements and

98      sampling.

99           Before the waveform can be retracked the first surface return (first major peak) is

100     identified within the range gate window. A copy of the waveform is heavily smoothed to remove

101     small-scale surface roughness signals, keeping the overall surface signal intact. The range gate

102     index of the first peak from the copy is then used to extract the leading edge of the original low

103     pass filtered waveform. Only leading edges with a peak index above 20 are used in the

104     retracking, as peaks before or after that indicate troublesome surface ranging. The extracted

105     leading edge is then oversampled by a factor of 100 (c.f. (Gray et al., 2013; Helm et al., 2014),

106     and the range $R$ between the surface and satellite is determined based on the 20% threshold

107     computed according to Davis et al. (1997). The range is then corrected for several atmospheric

108     and geophysical effects relevant to land ice studies according to Bouzinac (2014). The surface

109     elevation $H$ of the topography, relative to the WGS84 ellipsoid, is estimated as $H = A - R$, where

110     $A$ is the altitude of the satellite.

111          The measured surface return over a sloping surface does not originate from the

112     satellites nadir location, but from the "Point Of Closest Approach" (POCA) to the spacecraft

113     (Brenner et al., 1983). These off-nadir returns can introduce a large range bias to the surface,

114     depending on the magnitude of surface slope, ranging from 0-120 m (Brenner et al., 1983) as

115     the measured surface height is mapped to an erroneous position (i.e. the nadir position). To

116     mitigate the effect of this error we correct the measured range and location to the POCA point

117     using an a-prior DEM, following the approach of Bamber (1994). In contrast to previous studies

118     we account also for the local surface curvature, as Remy et al. (1989) showed that accounting

119     for surface curvature in addition to surface slope significantly improve results. The surface

120     slope, aspect and curvature are estimated from an a priori DEM. The GIMP elevation model

121     (Howat et al., 2014) was used to derive surface parameters for the slope-induced error

122     correction in the LRM mode. The DEM was resampled to 2 km resolution, using bilinear

123   interpolation, prior to parameter estimation, corresponding to the pulse-limited footprint of the

124   LRM mode.

## 2.2 - Interferometric Synthetic Aperture Radar Mode (SIN)

126   The SIN mode is used over the marginal areas of the ice sheets and other smaller glaciated

127   areas. In these areas the SIRAL altimeter operates as a Doppler/Delay radar system (Raney,

128   1998). The Doppler/Delay radar allows for higher along-track resolution compared to

129   conventional altimetry, resulting in 350 m resolution in along track and 1500 m across track. In

130   ordinary SAR operation only the amplitude of the radar echo is measured and the phase content

131   is discarded or ignored. With the inclusion of a second antenna on CryoSat-2, interferometric

132   SAR can also be performed. Difference in the path length between the POCA and the individual

133   antennas introduce a phase shift between the two retrieved signals that can be related to the

134   angle of arrival (look angle). The look angle can in turn be used to resolve the across track

135   (across antenna) location of the echo.

136       Multi-look processing is applied to ESA's L1B waveform product (Bouzinac, 2014) to

137   reduce the noise in the SIN waveform but it is still affected by speckle-noise, as is the case for

138   the LRM waveforms. To mitigate this effect, and to help identify the leading edge of the first

139   return, we apply speckle reduction filtering and leading edge extraction of the SIN waveforms in

140   the same way as for the LRM processing with minor changes due to differences in range gate

141   resolution. In this case, compared to the LRM retracking algorithm, only leading edges with a

142   peak index in the range of 20-350 are used for retracking the radar waveform.

143       The estimated coherence $C$ of the multi-looked waveforms is then filtered in two stages;

144   (i) all coherence measures larger than one is set to zeros (larger than one coherence exists in

145   the L1B product reason unknown). (ii) The coherence array, as a function of range, is filtered

146   using a 2D 5x5 Wiener filter to remove high frequency noise. The filtering of the waveform and

147    the coherence is applied to remove noise in the recreation of the interferogram. This is further

148    discussed later.

149        The measured differential phase $\phi$ of the return signal is affected by phase ambiguities;

150    a sudden shift of $2\pi$ in the measured phase. To reduce phase noise and aid the phase, an

151    unwrapping of the radar interferogram $I$ is performed according to Gray et al. (2013):

$$I = P \cdot C \cdot e^{-i\phi} \qquad (1)$$

153    The interferogram is then filtered using a wavelet-based de-noising technique, where the real

154    and imaginary parts of the interferogram are filtered separately. The unwrapping of the

155    interferogram allows for indirect filtering of the phase, without being affected by the phase-

156    ambiguities. Phase filtering is an important consideration as it has a direct affect on accuracy of

157    the position of the ground echo. We selected a bi-orthogonal as the mother wavelet to produce

158    the wavelet coefficients decomposed into three levels. Soft thresholding was applied to detail

159    coefficients, using a heuristic threshold rule to remove noise at every level. This was done on a

160    line-by-line basis. The final filtered differential phase was then recovered by:

$$\phi_f = Re\{I_f\} + Im\{I_f\} \qquad (2)$$

162    To resolve the phase ambiguities the filtered phase measurements require unwrapping. The

163    phase unwrapping is done on a line-by-line basis in two directions starting from the center of

164    gravity of the waveform (Wingham et al., 1986).

165        The return power distribution of a Doppler/Delay radar system shows an important

166    distinction from those from conventional pulse-limited radar systems. Here, the point

167    corresponding to the mean surface is not located at the half-power point on the leading edge,

168    but rather closer to the maximum (Wingham et al., 2006a). Therefore a new retracker has been

169    developed, closely related to the one used in Gray et al. (2013), to allow for adaptive retracking

170    of the upper parts of the leading edge of the SAR waveform. The algorithm follows the main

171    concept of the threshold retracker, developed by Davis, (1997), but instead of a pre-defined

172    threshold it tracks the maximum gradient of the leading edge of the waveform. We refer to this

173    approach as that "Leading-edge Maximum Gradient retracker" (LMG).

174        The surface returns are geolocated using the across track look-angle $\theta$ estimated from

175    the differential phase at the retrackig point according to (Wingham et al., 2006a). This, in

176    combination with the viewing geometry, is used to define the location of the surface return on

177    the ground using basic across track interferometric principles. We correct $\theta$ for the

178    interferometer surface slope error by applying the look-angle scaling factor estimated in (Galin

179    et al., 2013).

180        The along-track differential phase estimate, interpolated to the retracking point, is

181    affected by phase ambiguities not corrected for during the phase unwrapping procedure. To

182    reduce residual phase ambiguities an a priori DEM (GIMP) is used to extract the DEM surface,

183    resampled to 500 m resolution (corresponding to the along-track sampling), elevations at the

184    nadir and echolocation using bilinear interpolation. Over a sloping surface the surface return

185    should always come from a position upslope from the nadir point. Therefore the following

186    relation must hold where ($H_{echo} > H_{nadir}$) or for a more practical application ($H_{echo} - H_{nadir}) > \varepsilon$,

187    where $\varepsilon$ is the uncertainty of the DEM used. If this relation is violated $2\pi$ is added or subtracted

188    to the individual along-track phase estimate, depending on the sign.

189        A final step is applied to correct for any lingering phase ambiguities not corrected by the

190    a priori DEM. This step uses the assumption that the along-track phase should follow a

191    consistent pattern over most part of the satellite ground track. Hence, any large discrepancies

192    from the overall pattern of the along-track phase would indicate an ambiguity. The ambiguity is

193    detected by computing the residuals of the along-track phase by removing a smoothed version.

194    If any of the residuals have a magnitude larger than $\pi$ it is considered ambiguous and thus

195    corrected by adding or subtracting $2\pi$.

196    3 - Surface elevation changes from CryoSat-2

197    3.1 – Surface fit method

198    The surface-fitting method is based on fitting a linear model to the elevations as a function of

199    time and space inside a search radius of 1 km (e.g., Howat et al., 2008; Moholdt et al., 2010;

200    Sørensen et al., 2011; Wouters et al., 2015). The linear model consists of a time-invariant

201    (static) bi-quadratic surface model to account for variable topography inside the search radius

202    and time-variant part used to extract the temporal change in elevation. The model consists of a

203    total of 7-parameter whereof six of the parameters (a-coefficients) describe the bi-quadratic

204    surface modeling function, *dh/dt* the linear elevation change rate, *t* time in decimal years, $t_0$ the

205    mean time inside the footprint and *ε* the residuals from the linear regression.

206    $$h(x, y, t) = a_0 + a_1 x + a_2 y + a_3 xy + a_4 x^2 + a_5 y^2 + \frac{\partial h}{\partial t}(t - t_0) + \varepsilon \qquad (3)$$

207    The algorithm estimates the elevation change at every echolocation (or grid-node if desired) in

208    the data set. In each solution the signal amplitude and phase are also estimated by fitting a

209    seasonal signal model to the surface-fit elevation residuals, according to:

210    $$\Delta h(t) = s_0 \cos(wt) + s_1 \sin(wt) + \varepsilon \qquad (4)$$

211    where *Δh* is the elevation residuals estimated from the plan-fit model, $s_{0,1}$ are the model

212    coefficients and t the time. The amplitude *A* is then defined as $A = \sqrt{s_0^2 + s_1^2}$ and the phase *P* as

213    $P = \tan^{-1}\left(\frac{s_1}{s_0}\right)$.

214    To remove outliers an iterative 3*σ*-filter is used in the full model solution, i.e. the

215    topography, trend and seasonal signal are removed, using a maximum of 5-iterations. For each

216    iteration residuals (full-model) with an absolute value larger than 10 m are removed, as

217    seasonal changes larger than 10 m are not expected (Moholdt et al., 2010; Qi and Braun,

218    2013). The data inside the 1 km cap is weighted according to their distance from the estimation

219    point according to:

220
$$W = \frac{1}{\left(1 + \left[\frac{d}{\rho}\right]^2\right)}$$
(5)

221 where $W$ is the estimated weight, $d$ the distance and $\rho$ the correlation or resolution parameter

222 set to 500 m. The weighting allows the solution to better reflect local signal dynamics at the

223 prediction point.

224

225      Local elevation time-series are further computed from the elevation residuals and

226 elevation trend from each solution, according to:

227
$$h(x, y, t) = (t - t_0) \cdot \frac{\partial h}{\partial t} + \varepsilon$$
(6)

228 where $t$ is the time epochs inside the search cap, $t_0$ is the mean time of $t$, *dh/dt* is the elevation

229 change rate and $\varepsilon$ is the elevation residual at each time epoch.

230      The elevation changes estimated from the surface-fitting method are then culled to

231 remove outliers before spatial gridding. Elevation changes with a regression error larger than 15

232 m a$^{-1}$ are removed. The resulting surface elevations are binned at 5-km resolution for outlier

233 editing purposes. For each cell the local spatial trend is modeled as a bilinear surface, and

234 removed. The residuals are then edited using an iterative $3\sigma$ filter until the RMS converges to

235 2%.

236 3.2 – Crossover method

237 The crossover method is used to derive surface elevation at the intersection point between an

238 ascending and descending satellite ground track separated in time (Brenner et al., 2007;

239 Khvorostovsky, 2012; Zwally et al., 1989). The surface elevations and times are then estimated

240 at the crossover location for each track by linear interpolation of the two closest data points. The

241 crossover height difference is then estimated by taking the height difference between the two

242 tracks according to:

243
$$\Delta h = h_2 - h_1 + \varepsilon \qquad\qquad (7)$$

244   were $h_1$ and $h_2$ are the surface heights at the crossover location at time epoch $t_1$ and $t_2$,

245   respectively, and $E$ is the random measurement error, including orbital, range and retracking

246   errors.

247       This approach produces crossover height differences with scattered time-epochs

248   ranging from 0-4 years. CryoSat-2 has a 369-day repeat orbit configuration with a 30-day sub-

249   cycle meaning that each crossover location will be revisited every 369 days and surrounding

250   area every 30 days. This produces annual and sub-annual crossover difference around each

251   crossover location. This fact is used to produce elevation change rates by incorporating all

252   multi-temporal crossover difference within a neighborhood of 2.5-km around each crossover

253   location. The elevation change is then estimated using the same procedure described for the

254   surface-fit method, except that a bilinear model is used to remove any spatial trends in the

255   topography of the crossover elevations according to:

256
$$dh(x, y, t) = a_1 x + a_2 y + \frac{\partial h}{\partial t}(t - t_0) \qquad\qquad (8)$$

257   where *dh* is the crossover height difference, *(t-t₀)* the time difference, *a₁* and *a₂* the across and

258   along-track slope and *dh/dt* the elevation change rate. This produces elevation changes

259   comparable in time and in spatial coverage with the surface-fit method. The same outlier editing

260   schemes is applied to the crossover elevation change rates as for the surface-fit method.

## 3.3 - Gridding of sparse elevation and elevation change data

262   The gridding is done in a polar-stereographic projection with a latitude of origin at 70°N, central

263   longitude of 45°W and origin at the North Pole. The projection is referenced against the WGS-

264   84 ellipsoid and the grid-resolution. The observations derived from the surface-fit are gridded at

265   a resolution of 1x1-km, due to the high spatial sampling.

266       The method of Least Squares Collocation (LSC), described in Herzfeld (1992) is used to

267   grid the observations onto a regular grid. LSC is similar to Kriging and allows for optimal

268    interpolation and merging of data with different accuracies, using their inherent covariance

269    structure. The LSC-algorithm uses the 25 closest data points in 8-quadrants surrounding the

270    prediction point to reduce spatial biasing. The prediction equation consists of two terms where

271    the first term is the actual prediction term and the second term accounts for the non-stationary

272    part of the data, as described by:

$$\hat{s} = C_{sz}(C_{zz} + N)^{-1}z + \left(1 - \sum (C_{sz}(C_{zz} + N)^{-1})\right) m(z)$$

273    were $C_{\hat{s}z}$ is the cross-covariance, $C_{zz}$ is the auto-covariance, $N$ the diagonal noise-matrix

274    consisting of the a priori RMS-error and $m(z)$ is the median value of the observations inside the

275    search neighborhood.

276        The covariance of the data inside the local neighborhood is modeled as a function of

277    distance away from the prediction point using a third-order Gauss-Markov model described

278    below.

279    
$$C(r) = C_0 \left(1 + \frac{r}{\alpha} - \frac{r^2}{2\alpha^2}\right) e^{\left(-\frac{r}{\alpha}\right)} \tag{10}$$

280    where $r$ is the separation distance, $C_0$ the local data variance and $\alpha$ is a scaling factor estimated

281    from the correlation length.

282        LSC interpolation provides a RMS-error for each prediction point estimated from the

283    modeled covariance of the data according to:

$$C_{\hat{s}} = C_0 - C_{sz}(C_{zz} + N)^{-1}C_{sz}^{T} \tag{11}$$

284    where the RMSE of the prediction equals to $\sigma_{\hat{s}} = (C_{\hat{s}})^{1/2}$ and where $C_{sz}^{T}$ is the transposed cross-

285    covariance matrix.

286        The elevation changes estimated from the surface-fit and crossover methods are

287    interpolated to a regular grid using their a priori error estimated from the LSC scheme. To avoid

288    unrealistically small errors, common in the regression errors estimated over flat terrain, a

289    minimum error threshold is applied. Error values smaller than a specific threshold are set to the

290    threshold value. The threshold value is representative of the overall precision of the elevation

291      changes over flat terrain and is set to 0.2 m a$^{-1}$. The data are then gridded using a 75 km

292      correlation length determined from the comparison of CryoSat-2 elevation to airborne

293      measurements (Section 5).

294      The LSC algorithm is also used to generate a DEM based on the surface elevations

295      generated from the surface-fitting algorithm. The surface elevations generated from the surface-

296      fit were used as input to the gridding-algorithm. The use of surface elevations from the surface-

297      fit provides several advantages compared to the raw observations as they: provide an almost

298      equal number of observations as the raw data, have been screened for gross outliers, have

299      been low-pass filtered using the 1-km search radius, and are all reference to the same time

300      epoch. Further the RMSE error generated from the surface-fit estimated surface height can be

301      used as an a priori error for the LSC gridding procedure.

302      The DEM is generated using the same approach as for the surface elevation changes,

303      as described previously in the section. Before the gridding procedure is applied elevations $H < 0$

304      and $H > 3350$ m are removed from the data set. Further, elevations with a standard error larger

305      than 30 m are also removed. The elevations are binned spatially into a resolution of 1000 m and

306      inside each cell the local surface trend is removed by fitting of a planar surface, and an iterative

307      3σ filter is applied to the residuals to remove outliers.

## 308     4 - Surface elevations and elevation changes from ICESat

309    To assess basin-scale patterns of elevation change we compare elevation changes from

310    CryoSat-2 data to elevation changes derived from Ice, Cloud, and Elevation Satellite (ICESat)

311    data. Here we use release 33 (GLA06) data collected over the 2003-2009 period. The ICESat

312    surface heights were used to generate surface elevation changes and seasonal parameters

313    according to method M3 in Sørensen et al. (2011). The derived elevation changes were

314    corrected for the G-C offset (Borsa et al., 2014). Valid elevation retrievals were selected

315    according to Nilsson et al. (2015b). The ICESat elevation, seasonal amplitude and phase, are

316    then used for comparison with CryoSat-2 and to build continuous time series using the surface

317    fit method described in Section 3.1. For the purpose of this study no correction for the inter-

318    campaign bias was applied, as this is still an active area of investigation.

319    5 -Validation

320    Elevation and elevation change results were generated for the entire Greenland Ice Sheet using

321    CryoSat-2 data collected between Jan-2011 and Jan-2015 using the methodology presented in

322    (Sections 2-3) (JPL product) and by applying the methods of (Section 3) to ESA's CryoSat-2 L2

323    elevation products (ESA product). Surface elevations and elevation changes were validated

324    against airborne data sets obtained from NASA's Operation Ice-Bridge Airborne Topographic

325    Mapper (ATM), obtained from the "National Snow & Ice Data Center" (NSIDC) in the form of the

326    ILATM2 product. The generated elevation product has a resolution of 80 m, with a 40 m spacing

327    along-track. This mission produces both elevation and elevation changes with reported vertical

328    accuracy of ~10 cm and temporal accuracy in the cm-level (Krabill et al., 2002).

329        The derived surface elevations from CryoSat-2 are differenced against ATM surface

330    elevations within 50 m of each ATM locations. One month of CryoSat-2 data consistent in time

331    with the ATM elevations are used for the validation to avoid biases due to temporal sampling

332    and to obtain sufficient sample size. A total of four years of campaign data are used for the

333    validation of the surface elevations (2011-2014). The residuals are edited using an iterative $3\sigma$

334    filter to remove outliers. The accuracy and precision is estimated as the mean and standard

335    deviation of the differences, respectively. The residual distribution is further binned according to

336    surface slope estimated from the GIMP DEM (Howat et al., 2014) resampled to 500 m. The

337    sensitivity to surface slope (slope error) can be identified in the standard deviation of the binned

338    residuals and can be used to judge the quality of the produced surface elevation and elevation

339  changes, while the binned-average for the elevations can be used to determine radar-signal

340  penetration.

341     Surface elevation change rates estimated from three different time-periods (2012-2014,

342  2011-2013 and 2011-2014) of overlapping ATM observations (Krabill, 2014) are used to validate

343  the surface elevation changes estimated from the CryoSat-2 data. The same validation

344  methodology applied to surface elevations is applied to surface elevation changes, with a few

345  minor modifications. First the search radius is increased to 175 m to make it conform to the ATM

346  elevation change resolution of 250 m, as this search radius encloses the entire ATM grid cell.

347  Secondly the estimated mean and standard deviation are multiplied with the individual time-

348  intervals of the validation data sets to make the errors comparable.

349     For the surface-fit and crossover methods, near-coincident elevation change rates were

350  compared with ATM rates (e.g., April-2011 to April-2014). This provided three validation data

351  sets for the surface-fit method, due to its high spatial coverage. However, only the 2011-2014-

352  validation data set could be used for the crossover method, due to the lower spatial sampling of

353  the crossovers.

354     The overall accuracy and precision for both the surface elevation and elevations

355  changes are then estimated by taking the weighted mean, using the number of observations as

356  weights, for each data set giving an average error for each measurement mode, as seen in

357  Table-2. The weighted average errors for each mode and method have been summarized in

358  Table-1 and Table-2 for both the ESA's and our solutions, where the values for the individual

359  campaigns can be found in the Supplementary material.

360     The estimated surface elevation changes from the two independent methods were

361  validated separately using near-coincident ATM data. In general we find the same magnitude of

362  improvement observed in the surface elevation validation analysis. The statistics of the

363  elevation change validation have been summarized in Table-2 for each method independently

364  for the two modes of instrument operation. We find the lowest RMSE errors for the surface-fit

365    method, followed by the crossover method. This differs from the findings of Moholdt et al. (2010)

366    who found lower intrinsic errors for the crossover method, compared to the surface-fit method

367    when applied to ICESat data. The larger search radius used for our application of the crossover

368    method most likely explains the difference in findings between studies. Further, we find that the

369    surface-fit method provides the largest reduction in RMSE for the JPL product, corresponding to

370    40% and 55% for the SIN and LRM-mode, respectively.

371          The correlation length used to derive the number of un-correlated grid-cells, which is

372    used to estimate the standard error, was determined from a semi-variogram analysis of the

373    elevation change residuals from CryoSat-2 minus ATM using the data from the surface-fit

374    method. The comparison was done for each mode separately for all the individual campaigns

375    and multiplied with the their individual time span. The semi-variogram was then computed from

376    all the time-invariant residuals, to maximize the spatial coverage, for each mode. Analysis of the

377    semi-variogram showed approximate correlation lengths of 100 and 75 km for the SIN and

378    LRM-mode respectively. These correlation lengths are inside the range of the ones found by

379    Sørensen et al. (2011) for their analysis of ICESat data, which was found to be 50-150 km.

380          Although the main goal of this study is not to derive or compare different types of DEM's

381    they do play a critical part in removing the long-wavelength topography in order to derive the

382    monthly time-series of volume change from the DEM-method. To gain insight into the overall

383    quality of our CryoSat-2 derived DEM (referred to as JPL) we compare it to three other DEM's

384    derived from other data sets. Firstly, we compare it to a DEM derived from ESA CryoSat-2 L2

385    data (referred to as ESA) gridded in the same manner as our DEM (Section 3.3). Secondly we

386    compare it to a DEM from Helm et al. (2014), also based on CryoSat-2 data from 2011-2014

387    (referred to as AWI). Thirdly, we compare to a DEM from Howat et al. (2014) (which was used

388    to derive topographical parameters and corrections for the JPL CryoSat-2 data), based on

389    photogrammetry data from 1999-2002 co-registered to ICESat elevation data from 2003-2009

390    (referred to as GIMP).

391     These data sets were then compared to IceBridge ATM elevations, spanning the four

392     different campaigns previously used for validation of the CryoSat-2 elevations. The DEM

393     elevation was estimated at each ATM location, using bilinear interpolation, and the elevation

394     difference computed as (DEM-ATM). No attempt was made to account for differences in DEM

395     and ATM epochs. The estimation of the errors of the DEM was determined in the same way as

396     for the individual CryoSat-2 surface heights. The results of the comparison have been

397     summarized in Table-3, as the weighted average of the different campaigns. The values from

398     each individual campaign can be found in the supplementary material.

399     Analyzing the overall RMSE we find that the AWI produces the lowest RMSE, followed

400     by JPL, ESA and GIMP, due to AWI's lower standard deviation. However, the best accuracy is

401     obtained by the JPL DEM, which shows the lowest elevation bias of all DEM's. The ESA derived

402     DEM shows a slightly better standard deviation than the JPL DEM, which can be explained by

403     higher data density in the marginal areas for the ESA data. The difference in density is due to

404     the SNR rejection criterion applied in our elevation processing. This smoothing can explain the

405     lower standard deviations seen for the AWI product. The GIMP data set showed higher degrees

406     of impulse noise than the other products, explaining the higher observed standard deviation.

407     This impulse noise is attributed to that local elevation change rate, which was not accounted for

408     in the creation of the DEM (Howat et al., 2014). Overall we find that the JPL DEM provides a

409     suitable compromise between resolving of local detail and the minimization of bias. Further,

410     modification to the SNR filtering criteria will likely lead to additional improvements in the DEM.

411     To determine the effect of retracking on the accuracy and precision of the measured

412     surface heights from CryoSat-2 several tests was performed over different parts of Greenland

413     for both modes. Following the approach of Davis (1997) the accuracy (mean) and precision

414     (standard deviation) was computed as a function of leading edge threshold (in percent). This

415     computation was performed using a standard leading-edge threshold retracker, referred from

416     now on as LTH, for both the LRM and SIN mode independently. The validation was performed

417    in the same manner as described in Section 5, where ATM elevations from 2013 was used as

418    the surface reference.

419        For the LRM mode data from April 2013 from the northern parts of Greenland, spanning

420    the region 75-81°N and 54-44°W, was used to calculate height residuals for the different

421    thresholds. This produced approximately 1000 comparison locations, which was used to

422    calculate statistics. The same procedure was performed over Jakobshavn Isbræ, using the

423    same time span, to calculate statistics for the SIN-mode providing roughly 2500 comparison

424    locations.

425        The results of this analysis, summarized in Figure-2, show that for the LRM-mode that

426    the precision (as a function of threshold) follows the same behavior as observed by Davis

427    (1997), with a decrease of precision following increasing retracking threshold. However, the

428    most notable finding was the observed inverse relationship in precision for the SIN-mode

429    compared to LRM. For LTH-algorithm, in the SIN-mode, we observe a clear increase in

430    precision as the retracking threshold increases, seen in Figure-2, stabilizing around 30-40%.

431    Analyzing the accuracy derived from the different thresholds a clear difference in apparent

432    penetration depth of the radar signal can be observed for the two modes. For the SIN-mode,

433    below 40%, a positive bias is observed indicating that retracker produces elevations larger than

434    the corresponding airborne measured heights. For thresholds larger than 40% surface

435    penetration of the signal is observed which are in general closer to the surface compared to the

436    LRM-mode. We attribute this to differences in the near-surface density structure covered by the

437    two modes.

438        In general we conclude that for the LRM-mode that low retracking thresholds (0-30%)

439    reduces the magnitude of the apparent surface penetration bias and provides higher precision

440    compared to higher thresholds. Therefore, a threshold of ~20% of the leading edge is

441    suggested for retracking surface elevations for the LRM-mode, which was also previously

442    suggested by Davis (1997) and Helm et al. (2014). However, for the SIN mode a threshold

443    below 40% is not recommended, as this produces a clear positive elevation bias and poor

444    precision, as seen in Figure-2. Analyzing the difference between the LTH and the adaptive LMG

445    algorithm, used in the SIN-mode, we find that the LMG algorithm produces superior results in

446    precision compared to the standard LTH-algorithm. Comparing the adaptive solution from LMG

447    to the optimum threshold found by the LTH-algorithm, we find a comparable magnitude of the

448    elevation bias and a 32% improvement in precision, with an overall 27% reduction in RMSE,

449    using the LMG-retracker.  Studying the results from this comparison between the two-retracker

450    algorithms we recommend the use of the adaptive threshold approach, as it produces an

451    elevation repeatability that exceeds that of the standard threshold retracker and provides a low

452    penetration bias.

453        A case study was also performed to determine the different processing steps affect on

454    the quality of the retrieved observations. For this purpose the Barnes ice cap, on Baffin Island in

455    the Canadian Arctic, was chosen due to its small size, excellent validation coverage and due to

456    that it consist mostly of super-imposed ice (reducing radar signal penetration). The ice cap saw

457    a major IceBridge ATM campaign in 2011 providing a large number of flight tracks (spanning in

458    both North-South and East-West directions) suitable for validating CryoSat-2 data. The result of

459    this case study, which is detailed in supplementary material (i.e. Table-S1) shows that the

460    filtering of the differential phase has the highest impact on the overall accuracy of the

461    observation, reducing the RMSE with 12%, followed by the ambiguity correction. This shows the

462    importance of these steps, as they can have important implications for the overall quality of the

463    retrieved elevations. This especially true in high relief areas where small changes in the look

464    angle, or introduced phase ambiguity, can produce large elevation errors ranging from 0-100 m

465    in elevation (Brenner et al., 1983).

466

467 ## 6 - Error analysis

468 To compute volume change errors for the three methods we divide the error budget into two

469 main components (1) the observational error ($\varepsilon_{obs}$) and the interpolation error ($\varepsilon_{int}$).

470 The observational error budget is estimated using the root-mean-square error (RMSE) of the

471 difference between CryoSat-2 and airborne elevation change differences, as described in

472 Section 5. The RMSE is estimated separately from the two different modes, with the total

473 volume change error being computed as the RSS of standard error of the two modes, according

474 to:

475
$$\varepsilon_{vol} = \sqrt{(\varepsilon_{lrm} \, A_{lrm})^2 + (\varepsilon_{sin} \, A_{sin})^2} \qquad (12)$$

476 were $A_{lrm}$ and $A_{sin}$ are the corresponding areas covered by each mode. The $\varepsilon_{lrm}$ and $\varepsilon_{sin}$ are the

477 standard errors of the LRM and SIN computed from the airborne validation data sets.

478 The observational elevation change error is estimated from the residual elevation

479 change differences in Table-2 for the two methods. The RMSE from the LRM/SIN errors are

480 computed using Gaussian error propagation producing an observational elevation change error

481 ($\varepsilon_{obs}$). For the surface-fit and the crossover method the interpolation error is estimated as the

482 RMS of the LSC uncertainty grid. The final elevation change error is then estimated by combing

483 the two error sources using RSS according to:

484
$$\varepsilon_{dh/dt} = \sqrt{\left(\frac{\sigma_{obs}}{\sqrt{N}}\right)^2 + \left(\frac{\sigma_{int}}{\sqrt{N}}\right)^2} \qquad (13)$$

485 Here, $N$ is the number of uncorrelated grid-cells estimated from empirical semi-variogram

486 analysis of the CryoSat-2 and airborne elevation change differences, and estimated according

487 to:

$$N = \frac{A}{\rho_c^2} \qquad (14)$$

488 were $A$ is the total area of the Greenland Ice sheet ($\sim 1.7 \times 10^6$ km$^2$) and the correlation length $\rho_c$

489 of 75 and 100 km for the LRM and SIN mode respectively.

490    7 – Results

491    The measured surface elevations from the two CryoSat-2 products (JPL vs. ESA) showed large

492    differences in both accuracy and precision of the elevation measurements, as seen in Table-1.

493    The average accuracy and precision for the LRM-mode from the two products showed values of

494    $0.00 \pm 0.43$ m and $-1.06 \pm 0.89$ m for the JPL and ESA products respectively. This corresponds

495    to an average reduction in RMSE of 68% for the JPL product compared to the ESA LRM L2

496    data. Further, our product shows a lower residual slope error (seen in Figure-1c below ~0.5°)

497    indicating a lower sensitivity to the degradation of performance as the surface slope increases.

498        Surface elevations generated from the SIN-mode showed the same type of improvement

499    as for the LRM-mode. Here, an average accuracy and precision was found to be $-0.52 \pm 0.58$ m

500    and $-0.90 \pm 1.05$ m for the JPL and ESA SIN elevation products respectively. This further

501    corresponds to a reduction in the average RMSE of 27% for the JPL product compared to the

502    ESA product. For the SIN-mode the JPL processing produces a slightly lower residual slope

503    error, compared to the ESA processor (seen in Figure-1c above ~0.5°)

504        Larger improvements can be observed if separating the RMSE into its mean and

505    standard deviation, corresponding to the accuracy and precision of the measurements. Using

506    these definitions the analysis found that there is a 45% and 52% increase in precision for the

507    SIN and LRM mode respectively, compared to the ESA L2 product, and a 42% and 99%

508    improvement in accuracy for the respective modes.

509        The estimated surface elevation changes generated from the surface-fit method also

510    showed improvement in the estimated accuracy and precision, as seen in Table-2. Here, a

511    overall improvement in RMSE of 55% and 40% in the LRM and SIN mode, respectively, was

512    found when comparing against ESA L2 generated elevation changes from the same method.

513    The average accuracy and precision, compared to ATM generated elevation changes, was

514    found to be $0.11 \pm 0.67$ m (LRM) and $0.30 \pm 0.58$ m (SIN) for the JPL derived changes. This

515 compared to 0.25 ± 1.51 m (LRM) and 0.34 ± 1.06 m (SIN) for the ESA derived changes. This

516 corresponds to an increase in elevation change accuracy of 56% and 12% for the LRM and

517 SIN-mode, respectively, for the JPL product compared to ESA L2 elevation changes. The

518 estimated elevation changes also show an increase in precisions for the JPL product of 56%

519 and 45% for the LRM and SIN-mode, respectively, compared to its ESA counterpart.

520 The implementation of the LMG SIN retracking algorithm was found to reduce noise in

521 the retrieved surface elevations compared to conventional threshold retracking. Though roughly

522 comparable in accuracy, the LMG shows overall higher precision over all comparable leading

523 edge thresholds. The adaptive nature of the algorithm provides improved estimates of surface

524 elevation and gives good trade-off between accuracy and precision.

525 The 20% threshold retracker implemented in the LRM-mode was also found to provide

526 improved estimates of surface elevation (both in accuracy and precision) compared to the

527 model-based ESA-L2 retracker. Further, it also showed lower sensitivity to the 2012 melt event,

528 due to the lower threshold used on the leading edge of the waveform.

529 The estimated elevation changes of the Greenland Ice Sheet, excluding the peripheral

530 glaciers, over the period January 2011 to January 2015 show significant differences between

531 products (JPL and ESA) in both spatial patterns and the total magnitude (Figures 3 & 4). The

532 estimated volume change rate from the surface-fit method is -289 ± 20 $km^3 a^{-1}$ for the JPL-

533 product and -224 ± 38 $km^3 a^{-1}$ for the ESA-product with a mean difference of 65 $km^3 a^{-1}$. The

534 surface-fit and crossover-method produced on the order of ~20 million and ~2.5 million usable

535 elevation changes, respectively, providing high spatial sampling. Due to the constraint put into

536 the JPL processor the ESA L2 data produced slightly more surface-fit observations (~10%), as

537 more surface elevations were accepted.

538 The ESA product produces a more positive elevation change pattern, which can be

539 attributed to the 2012 melt event that introduced a large positive bias with a magnitude of ~0.5

540 m (Nilsson et al., 2015). Larger differences in the marginal areas for the surface-fit methods are

541    also observed. These are particularly noticeable in eastern Greenland (near 73.5 degrees in

542    latitude Figure 3) where the ESA data shows marginal areas of rapid thinning that are not visible

543    in the JPL solution. The positive signal detected in the interior of the ESA surface-fit-solution

544    can also be found in the basin time series, correlating well with the timing of the summer of

545    2012 melt event. These results are in agreement with earlier work demonstrating the sensitivity

546    of the ESA retracker to the changes in the volume/surface scattering ratio (Nilsson et al., 2015).

547        The two volume change methods produce consistent results from JPL derived elevation

548    changes, with a difference of around 1 $km^3 a^{-1}$. The spread between volume change methods is

549    larger (50 $km^3 a^{-1}$) when using ESA L2 data. The larger discrepancy can mostly related to the

550    sensitivity of the various methods to the melt event. The surface-fit method produces the most

551    negative number (least affected by the melt event and the lowest estimated error) and is

552    therefore taken as the most reliable estimate for both the JPL and ESA solution.

553        Comparing the estimated volume change to other studies using CryoSat-2 we find that

554    the JPL product is less negative than that estimated by Helm et al. (2014): -375 ± 24 $km^3 a^{-1}$.

555    This difference can be attributed to difference in processing methodology and to the different

556    epoch of the data used by Helm et al. (2014) of January 2011 to January 2014. Using the

557    corresponding epoch the JPL data gives a volume change estimate, based on the surface-fit

558    method, of -353 ± 21 $km^3 a^{-1}$, well within the stated uncertainty of Helm et al. (2014).

559        To examine the regional behavior of volume change estimates of the Greenland Ice

560    Sheet, gridded values from the three methods were divided into 8-drainage basins according to

561    Zwally et al. (2012). When analyzing the volume change time-series at the basin scale clear

562    differences can be observed in the annual and inter-annual behaviors (Figure 4). The northern

563    and interior basins (1, 2, 7, 8) all exhibit large differences (Table 4: 0 - 30 $km^3 a^{-1}$) in the

564    estimated volume change rates due to changes in the scattering regime resulting from the 2012

565    melt event. In the majority of the southern basins (4, 5, 6, 7), located in areas with higher

566    precipitation, both products show good agreement in both trends and seasonal amplitude

567    estimated from the surface-fit method.

568        The amplitude of the seasonal signal (Equation 4) estimated from the surface-fit (SF)

569    method show large differences in both magnitude and spatial variability (Figure 5). For the

570    surface-fit method a difference in amplitude of 54% is observed between the ESA and JPL

571    products, corresponding to area-averaged amplitude of 0.17 m or the JPL product and of 0.37 m

572    for ESA product. The comparison with ICESat derived amplitudes from 2003-2009 estimated in

573    (Sasgen et al., 2012) using the same methodology as used here produced an area-averaged

574    amplitude of 0.13 m, which is in good agreement with the JPL derived amplitude. This

575    agreement is also spatially consistent, as seen in (Figure 5), indicating low sensitivity to

576    seasonal changes in scattering regime of the upper snowpack. The observed difference in

577    amplitude bias, taking ICESat as the true surface amplitude while acknowledging that no inter-

578    campaign bias has been applied and the differences in epochs, is 0.03 ± 0.13 m for the JPL

579    product and 0.21 ± 0.27 m for the ESA product. The smallest differences are observed at high

580    altitudes above 2000 m a.s.l., where the three data sets show almost constant amplitude of 0.1

581    m (ICE/JPL) and 0.2 m (ESA), providing a factor of two larger amplitude for the ESA product.

582    Below 2000 m a.s.l., corresponding well to the equilibrium-line-altitude (ELA) of the Greenland

583    Ice Sheet, a rapid increase in amplitude is observed for all products. This is especially true for

584    the ESA product, which increases its magnitude by a factor of two.

585        Analyzing the amplitude patterns on a regional drainage basin level (Figure 5c) we find

586    good agreement between JPL CryoSat-2 and ICESat amplitude with ESA data producing

587    consistently larger amplitudes. Regionally, the highest amplitudes can be observed in the SE of

588    Greenland in basins (3,4,5) and are consistent with regional precipitation patterns that show

589    high average precipitation in these areas (Bales et al., 2009; Ettema et al., 2009).

590        The seasonal phase of the peak in amplitude of the seasonal cycle is shown in (Figures

591    5b and 5c) and shows generally good agreement between the two products, providing the

592    timing of the maximum of the accumulation signal, before the onset of melt, to the months of

593    June/July for both JPL and ESA CryoSat-2 data sets. The ICESat derived seasonal phase

594    shows a higher dependence on elevation where the maximum of the accumulation signal is

595    found in late May below 2000 m and late July/August above 2000 m in elevation. The ICESat

596    discrepancies from the CryoSat-2 data are found in specific basins. Disagreements between the

597    retrieved phase of the peak amplitude from Cryosat-2 and ICESat data are due to differences in

598    temporal sampling as discussed in more detail in Section 8.

599         We used ICESat and CryoSat-2 derived surface heights to generate time series over

600    three regions in Northeast area of Greenland (Zachariæ Isstrøm, Nioghalvfjerdsfjorden and

601    Storstrømmen glaciers) for comparison purposes These areas have in recent time shown large

602    and rapid changes, which has been noted by, e.g., Khan et al. (2014). The selected areas were

603    defined using hydrological basins derived by Lewis and Smith (2009), seen in (Figure 6), and

604    were further divided into smaller areas around the termini to highlight performance for areas of

605    rapid change. The ICESat and CryoSat-2 surface heights were then used to generate annual

606    time-series from 2003-2015 using (Equation 6) in the surface fit method. The estimated 12 year

607    time series show overall comparable elevation change rates over both time periods, especially

608    in the terminus areas, providing confidence that CryoSat-2 can actually monitor changes in

609    these areas.

610

611

612

613

614

615    8 - Discussion

616    The CryoSat-2 processing methodology presented here is found to produce accurate and

617    precise measurements of ice sheet elevation and elevation change. The main improvements

618    have been introduced in the SIN processor with the inclusion of a new type of land ice retracker

619    (LMG), advanced phase filtering and the inclusion of a phase ambiguity correction scheme. This

620    processing approach decreased the RMSE in the surface height retrieval by approximately 27%

621    (45% and 42% improvement in precision and accuracy). This improvement further propagated

622    into the quality of the estimated elevation changes for the SIN-mode, with the same magnitude

623    of improvement (Table-2). The described SIN-processing also generated surface elevations and

624    elevation changes with lower sensitivity to the local surface slope, indicating a higher degree of

625    accuracy in the geo-location and surface range estimation.

626         The SIN processing methodology further includes a phase filtering and phase ambiguity

627    correction scheme. Visual inspections of a large number of tracks have shown more coherent

628    estimation of the surface locations in our product and further the implementation of the phase-

629    ambiguity correction greatly reduced the number of track offsets. It was also noted that a

630    relatively course DEM (~1 km) could be used to resolve phase ambiguities. The detection and

631    correction of phase ambiguities are relatively straightforward and rely mostly on the relative

632    accuracy of the DEM. The implementation of the phase ambiguity correction is particularly

633    important when monitoring smaller ice caps and outlet glaciers, where frequent and large track

634    offsets can bias the estimation of the underlying topography.

635         The new LRM processing methodology focused on optimal retrieval of surface

636    elevations over the interior parts of the ice sheet. Here the choice of retracking threshold has

637    proven to be the critical factor to acquire high quality surface elevations and elevation changes.

638    The choice of 20% leading edge threshold level reduced the sensitivity to changes in the

639    scattering regime for low slope, high elevation areas. The functional-based retracking algorithm

640     used in the ESA LRM processor corresponds roughly to a 50% threshold level (Wingham et al.,

641     2006a), which appears to suffer from a higher sensitivity to changes in the scattering properties

642     (volume scattering) of the near-surface firn, as the range is reference higher up (later in time) on

643     the leading edge of the waveform. This effect can be seen in (Figure 2a), and that the observed

644     negative elevation bias (Table-1) for ESA-LRM (-1.0 m) fit well with the bias for the 50% LRM

645     threshold value shown in Figure 2a. This makes the algorithm more sensitive to annual and sub-

646     annual changes in snow-packs volume/surface scattering ratio, which can produce spurious

647     changes in elevation due to changes in the near surface dielectric properties. This is clearly

648     shown in patterns of ESA product derived elevation changes (Figure 3) where a large elevation

649     bias was introduced by the 2012-melt event (Nilsson et al., 2015a). The 20% threshold is less

650     sensitive to these types of changes (Table 1 & 2) and is in agreement with previous work that

651     has demonstrated that the 20% threshold best represents the mean surface inside the footprint

652     when exposed to a combination of surface and volume scattering (Davis, 1997).

653        Surface elevation changes, derived from multi-temporal radar altimetry observations, are

654     typically corrected for their correlation to changes in the radar waveform shape. This is to

655     reduce the effect of changes in the volume/surface scattering ratio of the ice sheets surface

656     (Davis, 2005; Flament and Rémy, 2012; Wingham et al., 2006b; Zwally et al., 2005). This

657     inherently adds to the complexity of the processing and analysis, introducing new biases and

658     error sources in the estimated parameters. For the processing approach presented here many

659     of these steps can be omitted or reduced, as they are an inherent part of the improved

660     waveform retracking. There have been attempts to remove spurious step-changes in elevation

661     resulting from sudden changes in surface scattering characteristics (caused by the 2012 melt

662     event) apparent in the ESA Baseline-B L2 data through post-processing strategies (Nilsson et

663     al., 2015c), but such approaches spread the bias over a longer period of time making the

664     "jumps" less noticeable in the time series by removing the step-change but introduces longer-

665    timescale bias of equal magnitude as the scattering layer is buried by less reflective snow and

666    low-density firn.

667         The result of the validation procedure shows a larger slope dependent bias in the ESA

668    data, both in the elevation and elevation changes (Figure-1). This is especially true for the

669    surface elevations, which can be seen in the figures of precision and accuracy (Figure 1a and

670    1c), where both figures show clear linear slope for the ESA surface heights. In comparison,

671    estimated elevations from JPL-product show relatively stable statistics over the entire slope

672    range above 0.2°. The validation of the estimated surface elevation changes, seen in (Figure

673    1b) and (Figure 1d), shows the effect of the 2012 melt event on the ESA derived elevation

674    changes below 0.2°. Further, the accuracy of the ESA derived changes show a clear negative

675    trend as function of increased surface slope. The derived precision of the surface elevation

676    change increases dramatically above 0.5°, as more complex topography is measured.

677         The JPL CryoSat-2 processing methodology produces seasonal amplitudes that are in

678    good agreement with those derived from ICESat data, further indicating the processors abilities

679    to track real and physical changes of the ice sheets surface. The current ESA implementation

680    produces noisier estimates of elevation change, as indicated by the larger standard deviations

681    of the residuals in the ESA solutions for the surface-fit and crossover-method. Figure 5 further

682    shows an amplitude bias in the ESA data compared to the corresponding ICESat reference

683    amplitudes. The bias is constant above the Greenland ELA located around 2000 m in altitude

684    but increases linearly as elevations decrease below this. The linear increase in amplitude

685    seems to be connected to the higher and more variable precipitation in the ablation zone where

686    changes in the variable snow cover produces changes in apparent surface height. This is less

687    prominent for the JPL SIN and LRM retrackers. The estimated seasonal phase in Figure 5c and

688    5d show that both JPL and ESA CryoSat-2 elevation products can adequately resolve the

689    seasonal maximum of the accumulation signal. Both products provide a timing of the maximum

690    to the month of July over the entire ice sheet, independent of elevation. Assessing the CryoSat-

691 2 derived maximum one does however notice a difference between CryoSat-2 and the

692 reference ICESat dataset. This constitutes roughly a ±1 month difference depending on the

693 elevation and the location. The cause of this difference can be attributed to the temporal

694 sampling of the ICESat mission. During the mission, due to degraded laser lifespan, data was

695 only collected in campaign mode during the spring and winter times corresponding to roughly

696 two months of measurements for each period. When the CryoSat-2 data was resampled to

697 coincide with the ICESat temporal sampling the same elevation and spatial pattern in the phase

698 of the maximum seasonal amplitude was observed as determined from the ICESat data. No

699 corresponding change in amplitude was observed. To mimic the temporal sampling of ICESat

700 the each year of the CryoSat-2 data was resampled using the total number of unique months in

701 the ICESat campaign record. This as the specific months used in the ICESat sampling changes

702 with different campaigns.

703    The two independent methods used to estimate the volume change of the Greenland Ice

704 Sheet produce consistent volume change estimates. This was especially true for volume

705 changes derived from the JPL elevations, with a discrepancy of less than 1 $km^3 a^{-1}$ between

706 methods. The two methods provided the same estimate of integrated volume change but the

707 use of the surface-fit is recommended as it produces higher spatial sampling compared to the

708 crossover-method and lower errors. The good agreement between the methods further

709 indicates a strong reliability in the estimated volume change rates of the Greenland Ice Sheet

710 over the four-year period. It also shows the ability of CryoSat-2 to capture both small and large-

711 scale spatial patterns in the rugged topography along the coastline and in the interior of

712 Greenland. This is especially true in the major outlet glacier systems (e.g., Zachariæ Isstrøm,

713 Nioghalvfjerdsfjorden and Storstrømmen).

714    Studying the northern parts of the Greenland Ice Sheet we find that CryoSat-2 captures

715 both intricate and complex behavior in the marginal areas of the ice sheet. This is exemplified in

716 the NE regions of Greenland (Figure 6) near Zacahariæ Isstrøm, Nioghalvfjerdsfjorden and

717    Storstrømmen, which all show complex and localized patterns of elevation change. Here,

718    Nioghalvfjerdsbrae shows very small changes in elevation during the observational time-span,

719    while Zacahariae Isstrøm, its major neighbor shows large negative trends in elevation change.

720    The observed behavior agrees with the observations made in recent studies by Khan et al.

721    (2014) and Mouginot et al. (2015) who document rapid retreat and drawdown of the ice-front

722    position of the two systems beginning in 2012. Storstrømmen outlet glacier system also appears

723    to show signs of rapid thinning at low elevations near the ice-front position while a large positive

724    signal is observed roughly 100 km upstream of the terminus. This pattern has also been

725    observed by Joughin et al., (2010) and Thomas et al., (2009), using airborne altimetry and

726    surface velocity mapping. Rates of elevation change from ICESat and CryoSat-2 data show

727    good agreement in basin-scale trends (Figure 6b,c).

728        The observed volume change rates estimated from this study are within the range of

729    previous studies, ranging from -186 to -309 $km^3 a^{-1}$ for the time period 2003-2009, summarized

730    by Csatho et al. (2014). A more recent study by Helm et al. (2014: -375 ± 24 $km^3 a^{-1}$) agrees

731    within uncertainties when differences in observation periods (2011 – 2014 vs. 2011 - 2015) are

732    taken into accounted. Assuming no changes in firn air content over respective study periods and

733    an ice density of 917 kg $m^{-3}$ we compare estimated changes with corresponding estimates of

734    mass change our estimated rate of Greenland glacier volume change. An assessment of

735    changes in firn air content is out of the scope of this paper. Velicogna et al. (2014) estimated

736    mass loss using the Gravity Recovery and Climate Experiment satellites (GRACE) over the

737    time-period 2003-2013 provided (converted from mass) a rate of -305 ± 63 $km^3 a^{-1}$ for the

738    Greenland which is inclusive of changes in Ice Sheet and peripheral glacier ice mass (–41 ± 8

739    $km^3 a^{-1}$, Gardner et al., 2013). The estimated volume change of -265 $km^3 a^{-1}$ from Csatho et al.

740    (2014) and the estimated rate of -305 $km^3 a^{-1}$ from Velicogna et al. (2014) spans our estimated

741    rate of -289 $km^3 a^{-1}$.

742    9 – Summary and Conclusion

743    We conclude that the use of an adaptive retracker for the SIN-mode, based on the maximum

744    gradient method, and the use of 20% threshold retracker for the LRM-mode provide improved

745    performance to the retracker currently used for the ESA L2 elevation products. It is further

746    important, especially for the SIN-mode, to apply a leading edge discriminator to identify and

747    track the leading edge of the waveform. The functional model currently employed in the ESA

748    processor has, to the author's knowledge, no such discriminator currently implemented. This is

749    important in the SIN-mode, as it often contains multiple surface returns. The single-return model

750    applied in the ESA processor will here have issues fitting a waveform containing multiple

751    surface returns resulting in retrack jitter (Helm et al., 2014).

752          Using the new CryoSat-2 processing methodology for the LRM and SIN-mode we

753    determine the volume change of the Greenland Ice Sheet to be -289 ± 20 $km^3 a^{-1}$ during the

754    period January 2011 to January 2015. The validation against airborne ATM surface elevations

755    and elevation changes showed an average improvement in the RMSE of the measured

756    elevations of 68% and 27% for the LRM and SIN mode respectively compared to ESA Baseline-

757    B L2 products. The new methodology also provide improved elevation changes with an

758    reduction in RMSE of 55% and 40% for the LRM and SIN mode respectively, compared to their

759    ESA L2 derived counterparts.

760          The methodology also showed less sensitivity to changes in near-surface scattering

761    properties than equivalent ESA products. The new processing methodology showed little effect

762    of slope-induced errors, providing better performance in the marginal areas of the ice sheets.

763    These improvements to the CryoSat-2 processing mitigate the need for post-processing to

764    correct correlations between changes in surface elevation and changes in the waveform shape

765    (i.e. backscatter and leading edge width etc.) that can introduce biases and add to the

766    complexity of the processing and analysis.

767    The presented CryoSat-2 processing methodology provides a lower intrinsic error in the

768    measured elevation, elevation change and volume change estimates, all of which will facilitate

769    improved understanding of the geophysical process leading to changes in land ice elevation.

770    Given the release of the ESA Baseline-C, which provides improved corrections and processing

771    mainly for the L1B product, further improvements are expected in the near future.

772    The complete set of grids used in this study is available for the public from the main author (J.

773    Nilsson) upon request and are provided in geotiff format.

## Acknowledgement

775    We are deeply thankful for the guidance of Laurence Gray and support of David Burgess. We

776    also thank Sebastian Bjerregaard Simonsen for very fruitful discussions. Further, we would also

777    thank and acknowledge Frank Paul at the University of Zurich for providing us with polygon-

778    outlines of the Greenland Ice Sheet and to the European Space Agency for providing their

779    CryoSat-2 L1b product. We thank the editor E. Berthier, the reviewer L. Schröder and the

780    anonymous reviewer for their valuable comments, which greatly helped to improve this

781    manuscript. This work was supported by funding from the NASA Cryosphere program. The

782    research was conducted at the Jet Propulsion Laboratory, California Institute of Technology

783    under contract with NASA.

784

785

786

787

788

789

## References

790 Abulaitijiang, A., Andersen, O. B. and Stenseng, L.: Coastal sea level from inland CryoSat-2

792 interferometric SAR altimetry, Geophys. Res. Lett., 42(6), 1841–1847,

793 doi:10.1002/2015GL063131, 2015.

794 Arthern, R., Wingham, D. and Ridout, A.: Controls on ERS altimeter measurements over ice

795 sheets: Footprint-scale topography, backscatter fluctuations, and the dependence of microwave

796 penetration depth on satellite orientation, J. Geophys. Res. Atmos., 106(D24), 33471–33484,

797 doi:10.1029/2001JD000498, 2001.

798 Bales, R. C., Guo, Q., Shen, D., McConnell, J. R., Du, G., Burkhart, J. F., Spikes, V. B., Hanna,

799 E. and Cappelen, J.: Annual accumulation for Greenland updated using ice core data developed

800 during 2000-2006 and analysis of daily coastal meteorological data, J. Geophys. Res. Atmos.,

801 114(6), doi:10.1029/2008JD011208, 2009.

802 Bamber, J. L.: Ice sheet altimeter processing scheme, Int. J. Remote Sens., 15(4), 925–938,

803 doi:10.1080/01431169408954125, 1994.

804 Borsa, A. A., Moholdt, G., Fricker, H. A. and Brunt, K. M.: A range correction for ICESat and its

805 potential impact on ice-sheet mass balance studies, Cryosphere, 8(2), 345–357, doi:10.5194/tc-

806 8-345-2014, 2014.

807 Bouzinac, C., CryoSat product handbook, European Space Agency, ESA, 2014.

808 Brenner, A. C., Blndschadler, R. A., Thomas, R. H. and Zwally, H. J.: Slope-induced errors in

809 radar altimetry over continental ice sheets, J. Geophys. Res., 88(C3), 1617,

810 doi:10.1029/JC088iC03p01617, 1983.

811 Brenner, A. C. ., DiMarzio, J. P. . and Zwally, H. J. .: Precision and accuracy of satellite radar

812 and laser altimeter data over the continental ice sheets, IEEE Trans. Geosci. Remote Sens.,

813 45(2), 321–331, doi:10.1109/TGRS.2006.887172, 2007.

814 Csatho, B. M., Schenk, A. F., van der Veen, C. J., Babonis, G., Duncan, K., Rezvanbehbahani,

815    S., van den Broeke, M. R., Simonsen, S. B., Nagarajan, S. and van Angelen, J. H.: Laser

816    altimetry reveals complex pattern of Greenland Ice Sheet dynamics., Proc. Natl. Acad. Sci. U. S.

817    A., 111(52), 18478–83, doi:10.1073/pnas.1411680112, 2014.

818    Davis, C. H.: Surface and volume scattering retracking algorithm for ice sheet satellite altimetry,

819    IEEE Trans. Geosci. Remote Sens., 31(4), 811–818, doi:10.1109/36.239903, 1993.

820    Davis, C. H.: A robust threshold retracking algorithm for measuring ice-sheet surface elevation

821    change from satellite radar altimeters, IEEE Trans. Geosci. Remote Sens., 35(4), 974–979,

822    doi:10.1109/36.602540, 1997.

823    Davis, C. H.: Snowfall-Driven Growth in East Antarctic Ice Sheet Mitigates Recent Sea-Level

824    Rise, Science (80-. )., 308(5730), 1898–1901, doi:10.1126/science.1110662, 2005.

825    Davis, C. H. and Ferguson, A. C.: Elevation change of the antarctic ice sheet, 1995-2000, from

826    ERS-2 satellite radar altimetry, IEEE Trans. Geosci. Remote Sens., 42(11), 2437–2445,

827    doi:10.1109/TGRS.2004.836789, 2004.

828    Ettema, J., Van Den Broeke, M. R., Van Meijgaard, E., Van De Berg, W. J., Bamber, J. L., Box,

829    J. E. and Bales, R. C.: Higher surface mass balance of the Greenland ice sheet revealed by

830    high-resolution climate modeling, Geophys. Res. Lett., 36(12), 1–5,

831    doi:10.1029/2009GL038110, 2009.

832    Flament, T. and Rémy, F.: Dynamic thinning of Antarctic glaciers from along-track repeat radar

833    altimetry, J. Glaciol., 58(211), 830–840, doi:10.3189/2012JoG11J118, 2012.

834    Galin, N., Wingham, D. J., Cullen, R., Fornari, M., Smith, W. H. F. and Abdalla, S.: Calibration of

835    the CryoSat-2 interferometer and measurement of across-track ocean slope, IEEE Trans.

836    Geosci. Remote Sens., 51(1), 57–72, doi:10.1109/TGRS.2012.2200298, 2013.

837    Gardner, A. S., Moholdt, G., Cogley, J. G., Wouters, B., Arendt, A. a, Wahr, J., Berthier, E.,

838    Hock, R., Pfeffer, W. T., Kaser, G., Ligtenberg, S. R. M., Bolch, T., Sharp, M. J., Hagen, J. O.,

839    van den Broeke, M. R. and Paul, F.: A reconciled estimate of glacier contributions to sea level

840    rise: 2003 to 2009., Science, 340(6134), 852–7, doi:10.1126/science.1234532, 2013.

841 Gray, L., Burgess, D., Copland, L., Cullen, R., Galin, N., Hawley, R. and Helm, V.:

842 Interferometric swath processing of Cryosat data for glacial ice topography, Cryosph., 7(6),

843 1857–1867, doi:10.5194/tc-7-1857-2013, 2013.

844 Gray, L., Burgess, D., Copland, L., Demuth, M. N., Dunse, T., Langley, K. and Schuler, T. V.:

845 CryoSat-2 delivers monthly and inter-annual surface elevation change for Arctic ice caps,

846 Cryosph., 9(5), 1895–1913, doi:10.5194/tc-9-1895-2015, 2015.

847 Helm, V., Humbert, A. and Miller, H.: Elevation and elevation change of Greenland and

848 Antarctica derived from CryoSat-2, Cryosph., 8(4), 1539–1559, doi:10.5194/tc-8-1539-2014,

849 2014.

850 Herzfeld, U. C.: Least-squares collocation, geophysical inverse theory and geostatistics: a bird's

851 eye view, Geophys. J. Int., 111(2), 237–249, doi:10.1111/j.1365-246X.1992.tb00573.x, 1992.

852 Howat, I. M., Smith, B. E., Joughin, I. and Scambos, T. A.: Rates of southeast Greenland ice

853 volume loss from combined ICESat and ASTER observations, Geophys. Res. Lett., 35(17), 1–5,

854 doi:10.1029/2008GL034496, 2008.

855 Howat, I. M., Negrete, A. and Smith, B. E.: The Greenland Ice Mapping Project (GIMP) land

856 classification and surface elevation data sets, Cryosph., 8(4), 1509–1518, doi:10.5194/tc-8-

857 1509-2014, 2014.

858 Joughin, I., Smith, B. E., Howat, I. M., Scambos, T. and Moon, T.: Greenland flow variability

859 from ice-sheet-wide velocity mapping, J. Glaciol., 56(197), 415–430,

860 doi:10.3189/002214310792447734, 2010.

861 Keith Raney, R.: The delay/doppler radar altimeter, IEEE Trans. Geosci. Remote Sens., 36(5),

862 1578–1588, doi:10.1109/36.718861, 1998.

863 Khan, S. a, Kjaer, K. H., Bevis, M., Bamber, J. L., Wahr, J., Kjeldsen, K. K., Bjork, A. a,

864 Korsgaard, N. J., Stearns, L. a, van den Broeke, M. R., Liu, L., Larsen, N. K. and Muresan, I. S.:

865 Sustained mass loss of the northeast Greenland ice sheet triggered by regional warming, Nat.

866 Clim. Chang., 4(4), 292–299, doi:10.1038/nclimate2161, 2014.

867  Khvorostovsky, K. S.: Merging and Analysis of Elevation Time Series Over Greenland Ice Sheet

868  From Satellite Radar Altimetry, IEEE Trans. Geosci. Remote Sens., 50(1), 23–36,

869  doi:10.1109/TGRS.2011.2160071, 2012.

870  Krabill, W. B., Abdalati, W., Frederick, E. B., Manizade, S. S., Martin, C. F., Sonntag, J. G.,

871  Swift, R. N., Thomas, R. H. and Yungel, J. G.: Airborne laser altimetry mapping of the

872  Greenland ice sheet : application to mass balance assessment, J. Geodyn., 34, 357–376,

873  doi:10.1016/s0264-3707(02)00048-0, 2002.

874  Lacroix, P., Dechambre, M., Legrésy, B., Blarel, F. and Rémy, F.: On the use of the dual-

875  frequency ENVISAT altimeter to determine snowpack properties of the Antarctic ice sheet,

876  Remote Sens. Environ., 112, 1712–1729, doi:10.1016/j.rse.2007.08.022, 2008.

877  Lewis, S. M. and Smith, L. C.: Hydrologic drainage of the Greenland Ice Sheet, Hydrol.

878  Process., 23(14), 2004–2011, doi:10.1002/hyp.7343, 2009.

879  Moholdt, G., Nuth, C., Hagen, J. O. and Kohler, J.: Recent elevation changes of Svalbard

880  glaciers derived from ICESat laser altimetry, Remote Sens. Environ., 114(11), 2756–2767,

881  doi:10.1016/j.rse.2010.06.008, 2010.

882  Mouginot, J., Rignot, E., Scheuchl, B., Fenty, I., Khazendar, A., Morlighem, M., Buzzi, A. and

883  Paden, J.: Fast retreat of Zachariae Isstrom, northeast Greenland, Science (80-. )., 350(6266),

884  1357–1361, doi:10.1126/science.aac7111, 2015.

885  Nilsson, J., Vallelonga, P., Simonsen, S. B., Sørensen, L. S., Forsberg, R., Dahl-Jensen, D.,

886  Hirabayashi, M., Goto-Azuma, K., Hvidberg, C. S., Kjaer, H. A. and Satow, K.: Greenland 2012

887  melt event effects on CryoSat-2 radar altimetry, Geophys. Res. Lett., 42(10), 3919–3926,

888  doi:10.1002/2015GL063296, 2015a.

889  Nilsson, J., Sandberg Sørensen, L., Barletta, V. R. and Forsberg, R.: Mass changes in Arctic ice

890  caps and glaciers: implications of regionalizing elevation changes, Cryosph., 9(1), 139–150,

891  doi:10.5194/tc-9-139-2015, 2015b.

892  Remy, F., Mazzega, P., Houry, S., Brossier, C. and Minster, J. F.: Mapping of the topography of

893    continental ice by inversion of satellite-altimeter data, J. Glaciol., 35(119), 98–107,

894    doi:10.3189/002214389793701419, 1989.

895    Remy, F., Flament, T., Blarel, F. and Benveniste, J.: Radar altimetry measurements over

896    antarctic ice sheet: A focus on antenna polarization and change in backscatter problems, Adv.

897    Sp. Res., 50(8), 998–1006, doi:10.1016/j.asr.2012.04.003, 2012.

898    Sasgen, I., van den Broeke, M., Bamber, J. L., Rignot, E., Sørensen, L. S., Wouters, B.,

899    Martinec, Z., Velicogna, I. and Simonsen, S. B.: Timing and origin of recent regional ice-mass

900    loss in Greenland, Earth Planet. Sci. Lett., 333–334, 293–303, doi:10.1016/j.epsl.2012.03.033,

901    2012.

902    Shepherd, A., Ivins, E. R., A, G., Barletta, V. R., Bentley, M. J., Bettadpur, S., Briggs, K. H.,

903    Bromwich, D. H., Forsberg, R., Galin, N., Horwath, M., Jacobs, S., Joughin, I., King, M. A.,

904    Lenaerts, J. T. M., Li, J., Ligtenberg, S. R. M., Luckman, A., Luthcke, S. B., McMillan, M.,

905    Meister, R., Milne, G., Mouginot, J., Muir, A., Nicolas, J. P., Paden, J., Payne, A. J., Pritchard,

906    H., Rignot, E., Rott, H., Sorensen, L. S., Scambos, T. A., Scheuchl, B., Schrama, E. J. O.,

907    Smith, B., Sundal, A. V., van Angelen, J. H., van de Berg, W. J., van den Broeke, M. R.,

908    Vaughan, D. G., Velicogna, I., Wahr, J., Whitehouse, P. L., Wingham, D. J., Yi, D., Young, D.

909    and Zwally, H. J.: A Reconciled Estimate of Ice-Sheet Mass Balance, Science (80-. ).,

910    338(6111), 1183–1189, doi:10.1126/science.1228102, 2012.

911    Sørensen, L. S., Simonsen, S. B., Nielsen, K., Lucas-Picher, P., Spada, G., Adalgeirsdottir, G.,

912    Forsberg, R. and Hvidberg, C. S.: Mass balance of the Greenland ice sheet (2003-2008) from

913    ICESat data - The impact of interpolation, sampling and firn density, Cryosphere, 5(1), 173–186,

914    doi:10.5194/tc-5-173-2011, 2011.

915    Sørensen, L. S., Simonsen, S. B., Meister, R., Forsberg, R., Levinsen, J. F. and Flament, T.:

916    Envisat-derived elevation changes of the Greenland ice sheet, and a comparison with ICESat

917    results in the accumulation area, Remote Sens. Environ., 160, 56–62,

918    doi:10.1016/j.rse.2014.12.022, 2015.

919    Thomas, R., Frederick, E., Krabill, W., Manizade, S. and Martin, C.: Recent changes on

920    Greenland outlet glaciers, J. Glaciol., 55(189), 147–162, doi:10.3189/002214309788608958,

921    2009.

922    Velicogna, I., Sutterley, T. C. and Van Den Broeke, M. R.: Regional acceleration in ice mass

923    loss from Greenland and Antarctica using GRACE time-variable gravity data, Geophys. Res.

924    Lett., 41(22), 8130–8137, doi:10.1002/2014GL061052, 2014.

925    Wenlu Qi and Braun, A.: Accelerated elevation change of Greenland's Jakobshavn glacier

926    observed by ICESat and IceBridge, IEEE Geosci. Remote Sens. Lett., 10(5), 1133–1137,

927    doi:10.1109/LGRS.2012.2231954, 2013.

928    Wingham, D. J., Rapley, C. G. and Griffiths, H.: New Techniques in Satellite Altimeter Tracking

929    Systems, in Proceedings of the IGARSS Symposium, Zurich, pp. 1339–1344, ESA SP-254,

930    Zurich., 1986.

931    Wingham, D. J., Francis, C. R., Baker, S., Bouzinac, C., Brockley, D., Cullen, R., de Chateau-

932    Thierry, P., Laxon, S. W., Mallow, U., Mavrocordatos, C., Phalippou, L., Ratier, G., Rey, L.,

933    Rostan, F., Viau, P. and Wallis, D. W.: CryoSat: A mission to determine the fluctuations in

934    Earth's land and marine ice fields, Adv. Sp. Res., 37(4), 841–871,

935    doi:10.1016/j.asr.2005.07.027, 2006a.

936    Wingham, D. J., Shepherd,  a, Muir,  a and Marshall, G. J.: Mass balance of the Antarctic ice

937    sheet., Philos. Trans. A. Math. Phys. Eng. Sci., 364(1844), 1627–35,

938    doi:10.1098/rsta.2006.1792, 2006b.

939    Wouters, B., Martin-Espanol, A., Helm, V., Flament, T., van Wessem, J. M., Ligtenberg, S. R.

940    M., van den Broeke, M. R. and Bamber, J. L.: Dynamic thinning of glaciers on the Southern

941    Antarctic Peninsula, Science (80-. )., 348(6237), 899–903, doi:10.1126/science.aaa5727, 2015.

942    Zwally, H. J., Bindschadler, R. a, Brenner,  a C., Major, J. a and Marsh, J. G.: Growth of

943    greenland ice sheet: measurement., Science, 246(4937), 1587–1589,

944    doi:10.1126/science.246.4937.1587, 1989.

945    Zwally, H. J., Giovinetto, M. B., Li, J., Cornejo, H. G. and Beckley, M. a: Mass changes of the

946    Greenland and Antarctica ice sheets and shelves and contributions to sea level rise: 1992-2002,

947    J. Glaciol., 51(175), 509, doi:10.3189/172756505781829007, 2005.

948    Zwally, H. J., Jun, L., Brenner, A. C., Beckley, M., Cornejo, H. G., Dimarzio, J., Giovinetto, M.

949    B., Neumann, T. a, Robbins, J., Saba, J. L., Donghui, Y. and Wang, W.: Greenland ice sheet

950    mass balance: distribution of increased mass loss with climate warming; 2003–07 versus 1992–

951    2002, J. Glaciol., 57(201), 88–102, doi:10.3189/002214311795306682, 2011.

952    Zwally, H. Jay, Mario B. Giovinetto, Matthew A. Beckley, and Jack L. Saba: Antarctic and

953    Greenland drainage systems, GSFC Cryospheric Sciences Laboratory, at

954    http://icesat4.gsfc.nasa.gov/cryo_data/ant_grn_drainage_systems.php, 2012

955   Tables:

956   *Table 1: Accuracy (Mean), precision (SD) and the total RMS-error (RMSE) of surface elevation*

957   *from CryoSat-2 observations compared to IceBridge ATM elevations. Here, the LRM mode*

958   *represents the interior of the ice sheet and SIN the marginal high relief areas.*

| JPL | Mean (m) | SD (m) | RMSE (m) |
|-----|----------|--------|----------|
| LRM | 0.00 | 0.43 | 0.45 |
| SIN | -0.52 | 0.58 | 0.82 |
| **ESA** | **Mean (m)** | **SD (m)** | **RMSE (m)** |
| LRM | -1.06 | 0.89 | 1.40 |
| SIN | -0.90 | 1.05 | 1.13 |

959

960   *Table 2: Accuracy (Mean), precision (SD) and the total RMS-error (RMSE) of surface elevation*

961   *changes from CryoSat-2 derived from two independent methods [Surface Fit (SF) an the*

962   *Crossover (XO) method], compared to IceBridge ATM data.*

| JPL - LRM | Mean (m) | SD (m) | RMSE (m) |
|-----------|----------|--------|----------|
| SF | 0.11 | 0.67 | 0.70 |
| XO | 0.24 | 0.72 | 0.78 |
| **ESA - LRM** | **Mean (m)** | **SD (m)** | **RMSE (m)** |
| SF | 0.25 | 1.51 | 1.57 |
| XO | 0.60 | 1.02 | 1.20 |
| **JPL - SIN** | **Mean (m)** | **SD (m)** | **RMSE (m)** |
| SF | 0.30 | 0.58 | 0.66 |
| XO | -0.60 | 1.26 | 1.26 |
| **ESA - SIN** | **Mean (m)** | **SD (m)** | **RMSE (m)** |
| SF | 0.34 | 1.06 | 1.11 |
| XO | -0.21 | 1.44 | 1.44 |

963
964

965 Table 3: Validation of four different DEMs, compared to IceBridge ATM elevation data. Based

966 on the weighted (number of samples) average of the four different ATM campaigns from 2011 to

967 2014. Elevation values at each ATM location were estimated by bilinear interpolation for each

968 DEM product.

| DEM | Mean (m) | SD (m) | RMSE (m) |
|---|---|---|---|
| AWI | -1.35 | 5.95 | 6.12 |
| GIMP | -1.13 | 7.22 | 7.32 |
| JPL | -0.87 | 6.31 | 6.39 |
| ESA | -2.83 | 6.13 | 6.76 |

969
970

971  *Table 4: Individual basin volume changes ($km^3a^{-1}$) for the Surface-Fit (SF) and Crossover (XO)*

972  *method for the JPL and ESA product for the time period Jan-2011 to Jan-2015, with*

973  *corresponding volumetric error.*

| Basin | SF – JPL | XO – JPL | SF - ESA | XO - ESA |
|-------|----------|----------|----------|----------|
| 1 | -26 ± 8 | -23 ± 12 | -9 ± 14 | -11 ± 15 |
| 2 | 5 ± 8 | 0 ± 13 | 31 ± 16 | 30 ±16 |
| 3 | -38 ± 9 | -34 ± 19 | -46 ± 16 | -31 ± 23 |
| 4 | -36 ± 7 | -37 ± 15 | -42 ± 12 | -16 ± 18 |
| 5 | -19 ± 4 | -27 ± 11 | -19 ± 7 | -6 ± 13 |
| 6 | -72 ± 7 | -71 ± 12 | -75 ± 13 | -79 ± 18 |
| 7 | -56 ± 7 | -51 ± 10 | -41 ± 14 | -35 ± 15 |
| 8 | -48 ± 8 | -45 ± 12 | -23 ± 15 | -27 ± 17 |
| **TOT** | **-289 ± 20** | **-288 ± 37** | **-224± 38** | **-174 ± 48** |

974

975    Figures:
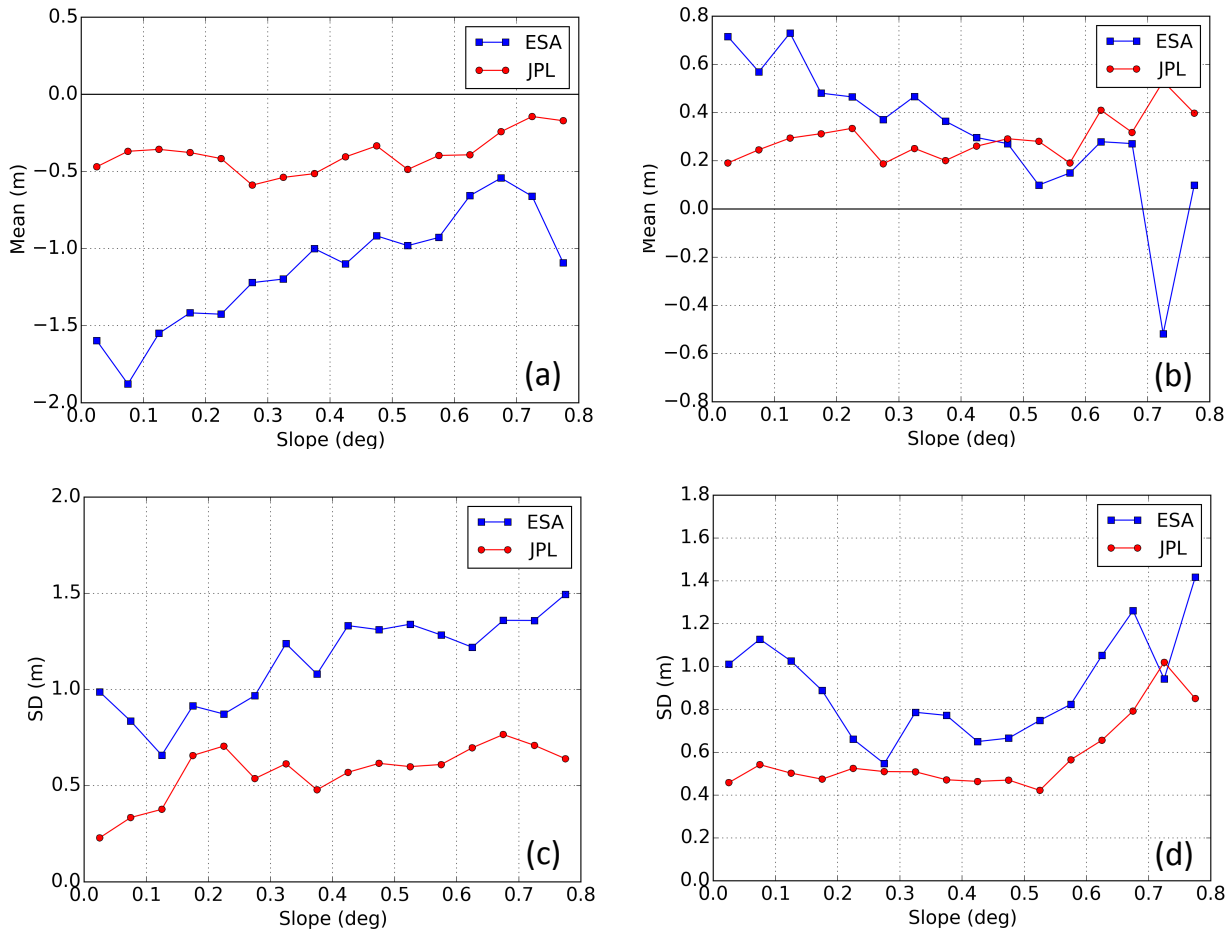
976

977    *Figure 1: Validation of surface elevations (2012) (a,c) and surface elevation changes (2011-*

978    *2014) (b,d) compared to IceBridge ATM, as a function of surface slope. The accuracy of the*

979    *measurement is defined as the mean-value (Mean) of the CryoSat-2-ATM residuals and the*

980    *precision as the standard deviation (SD).*

981

982

983

984

985

986
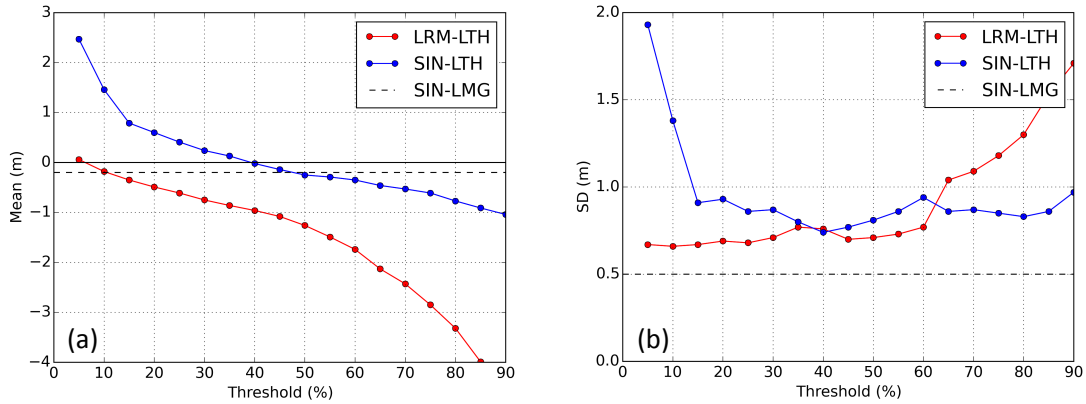
Figure 2: Accuracy (a) and precision (b) of JPL surface elevations, relative to near-coincident

ATM elevations, estimated from a Leading-edge Threshold retracker (LTH, dots) over

Jakobshavn and NE-Greenland and the Leading-edge Maximum Gradient (LMG retracker,

(dashed grey line) for the SIN-mode. The accuracy is defined as the mean-value (Mean) of the

CryoSat-2-ATM residuals and the precision as the standard deviation (SD).

994
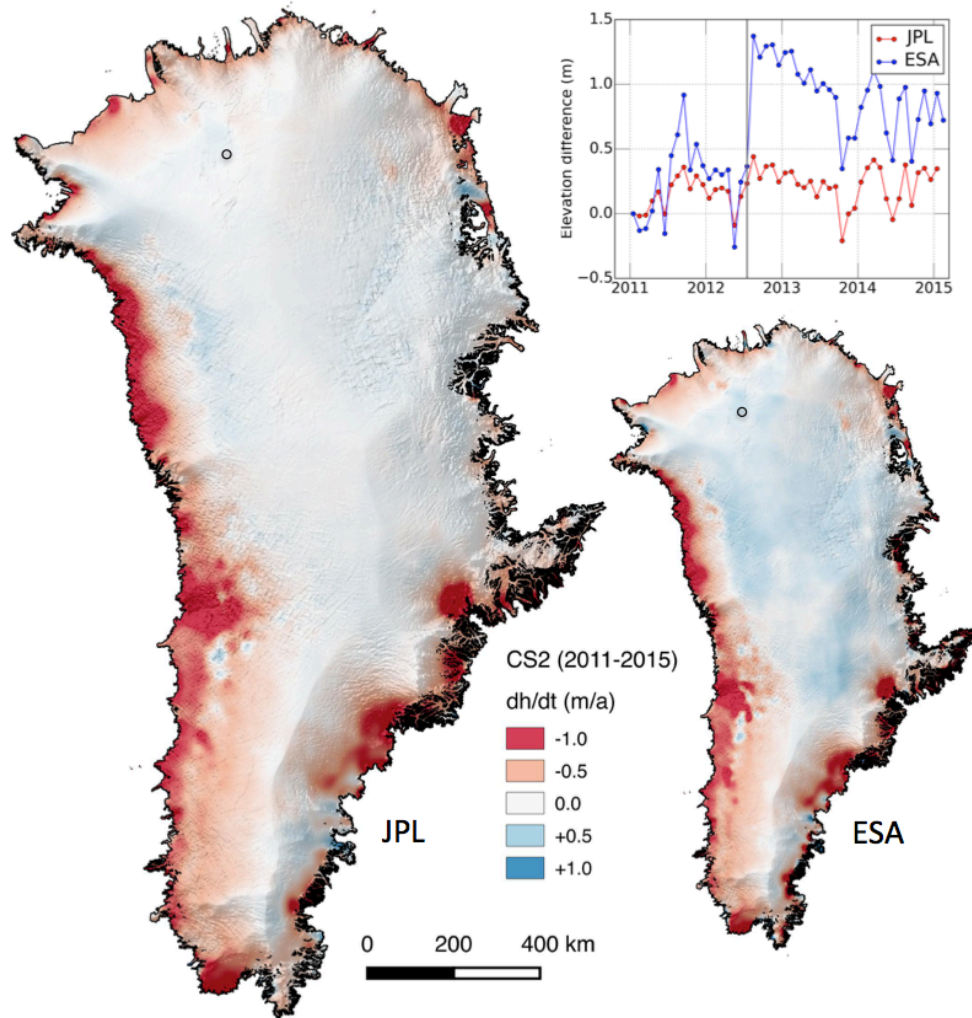
*Figure 3: 2011-2015 elevation changes estimated from the surface-fit methods for the estimated*

*L2 products. The time series depicted in the figure has been extracted from the NEEM camp*

*(77°27'N 51°3.6'W), indicated by the black circle. The time series show clearly the effect of the*

*2012 melt event, indicated by the grey vertical line, on the retrieved surface elevations. The JPL*

*product produced a total volume change of -289 ± 20 $km^3 a^{-1}$ while the estimated total volume*

*change of the ESA product totaled -224 ± 38 $km^3 a^{-1}$. This corresponds to -29 versus 38 $km^3 a^{-1}$*

*(H > 2000 m) and -259 versus -262 $km^3 a^{-1}$ (H < 2000 m) for the JPL and ESA product*

*respectively. Images have been smoothed with a 10 km median filter for visualization purposes.*

*The 1x1 km ice sheets mask used in this figure was constructed from polygons obtained from*

*Frank Paul at the University of Zurich (personal communication).*
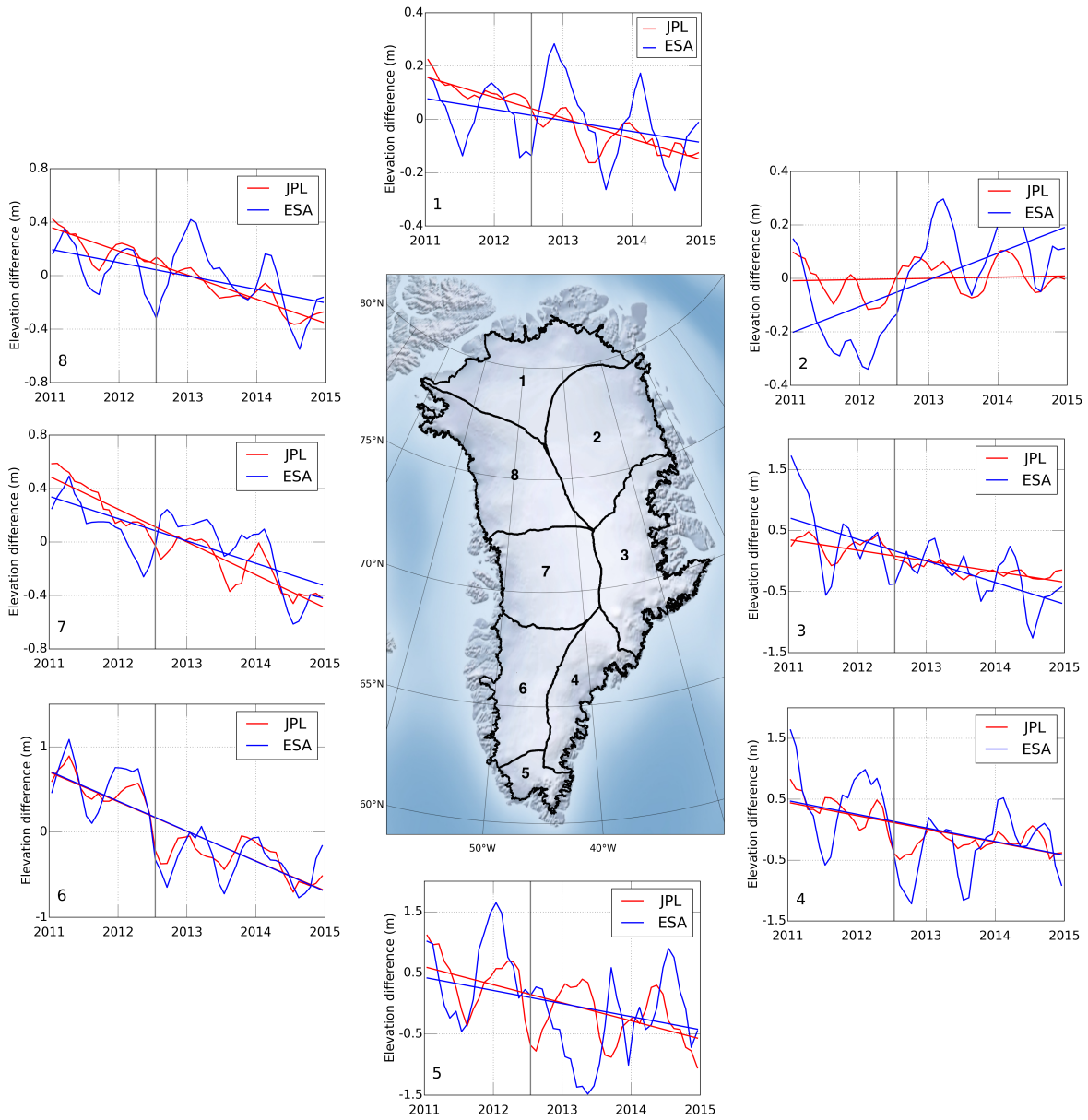
1005

Figure 4. Monthly elevation change time-series for 8 large drainage basins of the Greenland Ice

1006

Sheet. Time-series have been smoothed using a 3-month moving average for improved

1007

visualization. The grey vertical line indicates the timing of the 2012 melt event.

1008

1009

1010

1011    *Figure 5: Estimated seasonal amplitude (a,c) and phase of the maximum amplitude (b,d) from*

1012    *the surface-fit method for CryoSat-2 [ESA (blue) and JPL (red)] compared to ICESat (ICE,*

1013    *black)). Values are compared using a search radius of 500 m, using the closest point within this*

1014    *distance, and the phase offset is referenced from 1$^{st}$ of January. The values of amplitude and*

1015    *phase are then binned according to elevation using the median value within 100 m intervals.*

1016

1017

1018

1019

1020

1021

1022
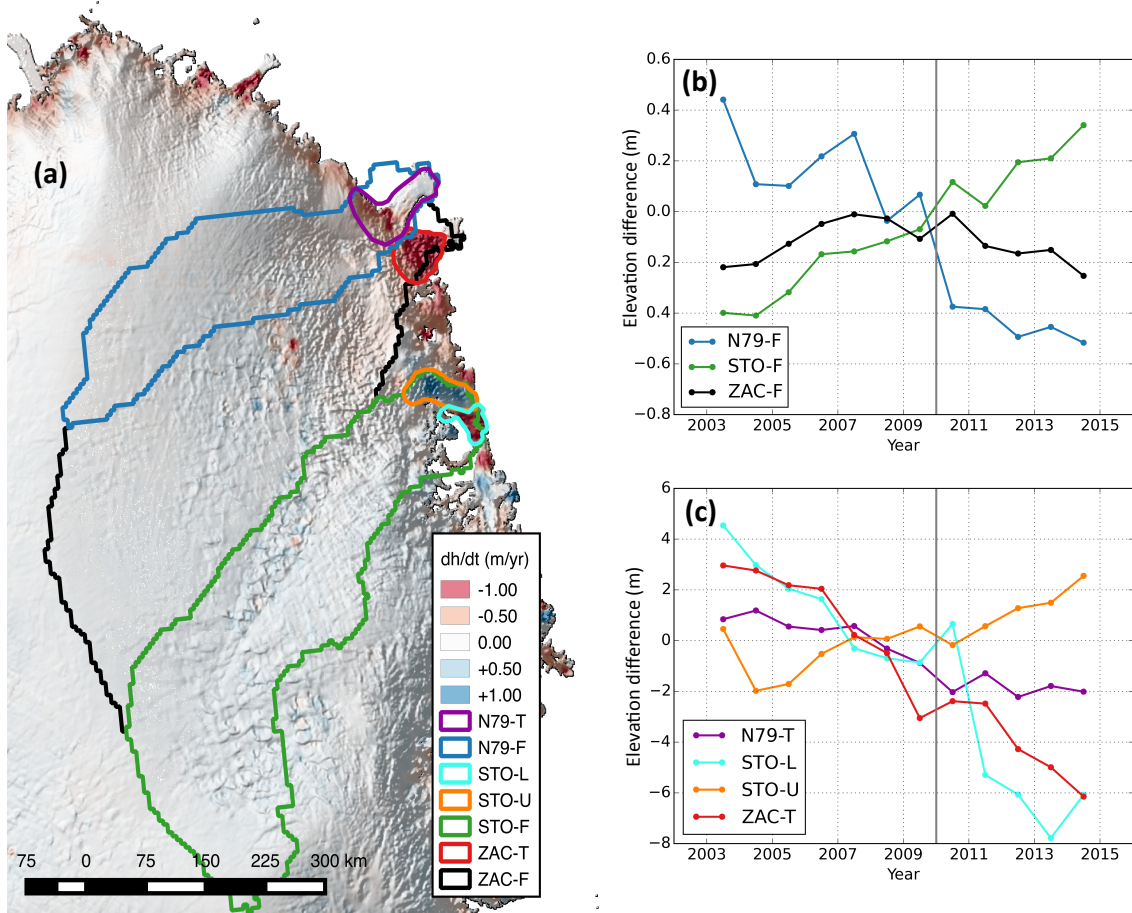
1023

1024    *Figure 6: Northeast part of the Greenland Ice Sheet showing surface elevation change (a) from*

1025        *CryoSat-2 JPL-solution (2011-2015), with corresponding hydrological basin outlines. The*

1026    *hydrological basins are separated into full basins size (b) and to the terminus areas (c). Sub-*

1027        *figures (b) and (c) shows a merged 12 year annual elevation time series from ICESat and*

1028    *CryoSat-2 for each color-coded area in (a). The derived elevation time series was formed using*

1029    *the surface-fit method described in Section (3.1). The elevation change map is overlaid onto the*

1030        *CryoSat-2 hill shaded DEM based on surface heights from Jul-2010 to Feb-2015.*

1031

1032